Oriented and Continuous Phase Epitaxy Enabled by A Highly Dendrite-Resistant Plane towards Super-High Areal Capacity Zinc Metal Batteries

Yangyang Wang, Chunxia Chen, Ao Xu, Jiaxin Lv, Miao Huang, Tiantian Ren, Jinbo Bai, Hui Wang, Xiaojie Liu

Oriented and Continuous Phase Epitaxy Enabled by A Highly Dendrite-Resistant Plane towards Super-High Areal Capacity Zinc Metal Batteries

Yangyang Wang[1], Chunxia Chen[1], Ao Xu[1], Jiaxin Lv[1], Miao Huang[1], Tiantian Ren[1], Jinbo Bai[2], Hui Wang[1] and Xiaojie Liu[1]*

[1] *Key Laboratory of Synthetic and Natural Functional Molecule of the Ministry of Education, College of Chemistry & Materials Science, Northwest University, Xi'an 710127, P. R. China*

[2] *Laboratoire Mécanique des Sols, Structures et Matériaux (MSSMat), CNRS UMR 8579, Ecole CentraleSupélec, Université Paris-Saclay, 8-10 rue Joliot-Curie, 91190 Gif-sur-Yvette, France*

* Corresponding Author:

E-mail address: xiaojie.liu@nwu.edu.cn (X. Liu)

Abstract:

Unstable Zn metal anodes with dendrites/side reactions are becoming the main obstacle to the practical application of zinc-based aqueous batteries. Epitaxial growth has been considered to be an effective strategy for solving these issues, especially for inducing the (002) plane growth. Nonetheless, the (002)-textured Zn is difficult to achieve highly stable Zn anode under high capacity resulting from its large lattice distortion. Herein, the Cu single atom anchored polymeric carbon nitride (Cu@PCN) is synthesized by a facile thermal polymerization method. Serving as multifunctional protective layer on Zn surface, the Cu@PCN can provide massive nucleation sites at a nano-level and uniformize the electron distribution through coordination engineering. Optimizing the coordination structures of single Cu and N atoms within the carbon matrix enables a redistribution for electric field and regulates ion flux. More importantly, this coordination strategy with single atoms is first reported to customize oriented and continuous phase epitaxy along highly dendrite-resistant Zn(101) plane by reducing (101) surface energy. This pattern of oriented dense deposition leads to stable and reversible Zn plating/stripping is achieved, which delivers an extended cycling life of 550 h at 10 mA cm^{-2}, 20 mAh cm^{-2}. The practical full cell also displays stable performance for 1200 cycles.

Keywords: dense Zn anodes; high capacity; dendrite-resistant plane; coordination engineering; preferential growth

1. Introduction

Aqueous zinc-ion batteries (AZIBs) have long been heralded due to their attempting features including low cost, high safety, and facile manufacture, which are thought as one of the promising alternatives for lithium-ion batteries in large-scale energy storage systems.[1] However, the practical application of AZIBs is mainly limited by the several major flaws related to zinc metal anode, involving intractable dendrite growth, chemical/electrochemical side reactions, and H_2 evolution reaction during the Zn plating/stripping process, which have rendered poor Coulombic Efficiency (CE) and severely limited long-term operation of Zn metal-based batteries.[2] Therefore, it is crucial to suppress zinc dendrite and stabilize the zinc anode interface for the practical application of AZIBs.

The majority of current studies focuses on the anode structure, optimization of electrolyte composition and protective coating design to manipulate zinc deposition behaviors and facilitate the electrochemical stability of Zn anodes.[3] Among them, the construction of artificial protective layers (APLs) is deemed an effective and promising method owing to their inherent superiority in limiting the Zn dendrite growth by modulating the Zn^{2+} flux and the electric field distribution.[4] Regrettably, the indiscriminate regulation is not beneficial to suppressing side reactions and achieving homogeneous Zn deposition, and is also far from being able to cope with electrochemical polarization under high current densities.[5] Meanwhile, random direction of zinc deposits face challenges like dendrite growth, increasing short-circuit risks, electrode deformation and higher interface impedance.[6] Thus, designing sustainable coatings especially with reliable and precise regulation in zinc deposition under high current density is still highly desired. Among these feasible options, the rational design and fabrication of 3D conductive hosts has proven to be an effective strategy to regulate local current density and distribute a uniform electric field. To further improve the behavior of Zn deposition, zincophilic species (e.g., Cu, Sn and In) with high adsorbing ability for Zn^{2+} ions are usually introduced into the 3D conductive hosts to benefit Zn^{2+} ion nucleation and growth[7]. Unfortunately, previous

studies for metallic sites primarily focused on large-sized nanoparticles or clusters, contributing to an underutilized metallic site resulting from the inaccessible inner sites. Furthermore, they incline to exacerbate large-sized nuclei, which can further aggravate the uneven distribution of electric fields.[8] On the contrary, reducing the dimensions of metallic sites to the atomic scale (e.g., single metal atoms) and uniformly enclosing them within a host matrix can enhance site utilization and regulate the size of the nuclei.[9] Meanwhile, through coordination engineering, metal single atoms with adjustable coordination environments and metal-molecule interactions help modulate charge distribution around the active center.[10] For example, Yu et al. demonstrated that atomically dispersed Co-N_3 sites exhibit excellent zincophilia and a strong charge polarization effect, enabling the redistribution of the electric field in the microspace and regulation of ion flux, thereby promoting uniform Zn deposition.[11] Consequently, single atoms with strong polarization fields could be incredible for regulating the electric field and inducing uniform Zn deposition under high current densities. Nevertheless, the exact coordination engineering of zincophilic sites on the atomic scale is still an unexplored frontier and needs further investigation.

In addition to hydrogen evolution and zinc corrosion, dendritic growth is a common problem that can lead to cell failure due to internal shorting. Recent research has emphasized the orientation of crystal planes plays a crucial role in determining the morphology of zinc deposits. At present, numerous studies have demonstrated that owing to the uniform surface charge density and low surface energy, springing from equipotential arrangement structure of zinc atoms with high atomic packing density, the Zn (002) crystal plane has been regarded to have stronger ability against chemical corrosion and more significant anti-dendrite growth feature.[12] Additionally, the deposited zinc is more inclined to grow at a small angle along the Zn (002) direction, which enables the zinc metal with a compact and dendrite-free deposition layer.[3d] Based on these advantages, almost all endeavors have been devoted to designing practicable texturing strategies to manipulate the preferred Zn (002) orientation deposition, thereby achieving dendrite-free growth on the zinc anode surface of

AZIBs with excellent plating/stripping stability.[13] Notwithstanding, due to the effect in weak bonding of Zn (002) on deposited atoms, Zn deposited on the texture (002) substrate can readily deviate from the original lattice growth, which leads to the accumulation of lattice distortion, and dendrites are eventually triggered on Zn electrode. Moreover, the gap lap pattern of sheet zinc results in ununiform electric field distribution at the interface, which exacerbates dendrite propagation and corrosion.[14] Consequently, (002) zinc deposits cannot maintain orientated and continuous phase epitaxy, limiting the ability to control deposited zinc with a super high areal capacity. By contrast, Zn (101) possesses a strong epitaxy effect, exhibiting a smooth surface and ordered deposition even at a high plating capacity due to its highly dendrite-resistant ability.[14] Meanwhile, the Zn (101) anode has a lower grain boundary area as well as higher hydrogen evolution energy barrier than Zn (002), which is reasonable to consider that the electrode delivers an excellent effect on inhibiting side reactions.[15] Thus, realizing controllable growth in which the highly dendrite-resistant Zn (101) plane dominates is of great significance for obtaining a super-high areal capacity Zn anodes. Ideally, the freshly electroplated zinc will sequentially build upon its inherent structure in an organized fashion, resulting in a tightly packed and densely deposited morphology. Nevertheless, the Zn (101) oriented deposition is still rather intractable, and the deposited zinc platelets gradually tend to randomly stack without a specific orientation due to the spontaneous 2D diffusion of zinc anode. In other words, the (101) crystal plane readily promotes the deposition along this direction into “tip-effect” sites, thereby developing into the zinc dendrite when the preferred (101) orientation is not fully arranged.[16] Unfortunately, so far little attention has been paid to the preferred orientation of Zn along the distinctive (101) crystal plane during the electroplating process. More importantly, there is no reported work about the oriented and continuous phase epitaxy along the highly dendrite-resistant (101) plane through the strategy of single atom coordination engineering. As a result, it is highly expected that designing a multifunctional interface with effect of single atom can achieve oriented dense and homogeneous deposition of zinc along the highly dendrite-resistant (101) facet towards super-high

areal capacity Zn metal batteries.

Herein, Cu single atoms anchored polymeric carbon nitride (denoted as Cu@PCN) has been designed and applied as a multifunctional coating with zincophilic and hydrophobic features for dendrite-free AZIBs. The construction of a zincophilic-hydrophobic layer can suppress the side reactions since the ion-sieving effect shielding the reactive water molecules. Cu species possesses a natural affinity for Zn^{2+}, which is crucial for the formation of a stable and effective protective layer on the zinc anode. Atomically dispersed Cu-N_3 sites in coordination engineering shows good zincophilia and strong charge redistribution effect, which can redistribute the electric field and regulate the ion flux. More importantly, this coordination engineering with single atoms is first reported to reduce the surface energy of the highly dendrite-resistant Zn (101) crystal plane, inducing preferentially crystallographic (101) orientation electroplating growth and facilitating oriented dense Zn deposition (Figure 1a). The Zn (101) plane can guide the nucleation and growth of zinc in a controlled planar method, this orientation promotes uniform and dense zinc deposition, which is essential for preventing dendrite growth and ensuring the long-term stability of zinc anodes. Benefiting from this unique growth pattern, the Cu@PCN-coated Zn (Cu@PCN-Zn) anode demonstrates remarkable reversibility in zinc plating/stripping, sustaining for 2000 h in Cu@PCN-Zn symmetric cells at 5 mA cm^{-2}/1.25 mA cm^{-2}. Interestingly, Cu@PCN-Zn endured cyclability for 240 h at a high rate of 1 mA cm^{-2} and 10 mAh cm^{-2} for plating/stripping cycles. Moreover, the rate capabilities and long-term cycle performances of Zn//MnO_2 full cells are considerably enhanced by the Cu@PCN-Zn anodes.

2. Results and Discussion

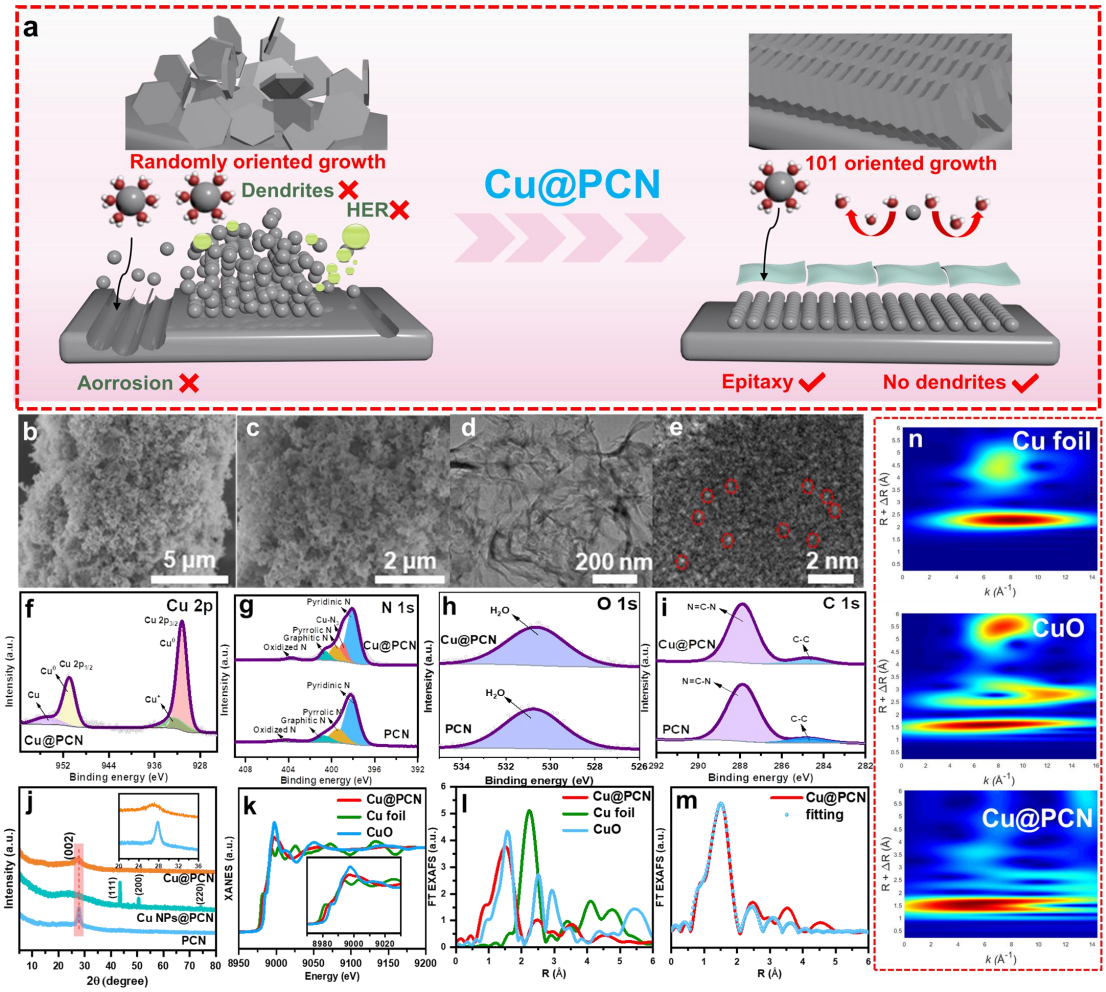

Figure 1. (a) Schematic illustrations of Zn metal plating behaviors on bare Zn and Cu@PCN-Zn electrodes. (b,c) SEM images of Cu@PCN. (d) TEM image of Cu@PCN. (e) HAADF-STEM image of Cu@PCN. XPS characterizations of PCN and Cu@PCN: (f) Cu 2p spectra, (g) N 1s spectra, (h) O 1s spectra and (i) C 1s spectra. (j) XRD patterns of PCN, Cu NPs@PCN and Cu@PCN. (k) The Cu K-edge XANES spectra, and (l) k^3-weighted $\chi(k)$-function of EXAFS spectra of Cu@PCN, Cu foil and CuO. (m) EXAFS fitting curves of Cu@PCN at *R* space. (n) WT contour plots of the EXAFS spectra of Cu@PCN, Cu foil and CuO.

As schematically illustrated in Figure S1, Supporting Information, using a facile thermal polymerization method, a family of atomic Cu anchored on N-doped carbon nanosheets (Cu@PCN) were successfully prepared. To gain deeper insights into the structure of Cu@PCN, the morphology of materials is firstly investigated under scanning electron microscopy (SEM) and transmission electron microscopy (TEM) images. The as-synthesized Cu@PCN nanocomposite shows a 3D interconnected

structure (Figures 1b–d) that consisted of nanosheets with highly wrinkled surface while no apparent Cu-containing nanoparticles or clusters, similar to the morphologies of pure PCN without Cu atoms and Cu NPs@PCN (Figure S2 and S3, Supporting Information). Isolated but uniform bright dots assigning to the Cu single atoms are clearly discerned in the high-angle annular dark field-scanning transmission electron microscopy (HAADF-STEM) image (Figure 1e), demonstrating the atomic mono-dispersity of Cu species in the carbon matrix. Meanwhile, the energy-dispersive X-ray spectroscopy (EDS) elemental mapping images as presented in Figure S4, Supporting Information clearly demonstrate the uniform dispersion of C, N and Cu elements in Cu@PCN. In addition, the loading of Cu in Cu@PCN is 1.25 wt%, as determined by the Inductively coupled plasma (ICP) measurements. This is also evidenced by the X-ray diffraction (XRD) pattern, in which there is no reflection peaks for metal-associated crystals. The XRD pattern of PCN consists of one strong diffraction peak at 27.5° and one very weak peak at 13.1°, can be identified to the (002) and (100) planes (Figure 1j). Meanwhile, the (002) diffraction peak of Cu@PCN shifts to a lower 2θ angle than PCN, indicating Cu-loading increases the interlayer spacing of PCN nanosheets.[17] In addition, the XRD pattern of Cu NPs@PCN can be identified as metallic Cu phase. X-ray photoelectron spectroscopy (XPS) survey spectrum reveals that Cu@PCN consists of C, N, O and Cu elements (Figures 1f–i and Figure S5, Supporting Information). High-resolution XPS Cu 2p spectrum displays four characteristic peaks, which corresponds to Cu $2p_{1/2}$ and Cu $2p_{3/2}$, respectively (Figure 1f). This means that Cu species is in an ionic state,[18] described in the form of Cu-N bonds. Meanwhile, in addition to the typical pyridinic N, pyrrolic N, graphitic N and oxidized N species, the N 1s fitting spectrum shows a significant contribution at 399.0 eV, ascribing to Cu-N, indicating the interaction between Cu and N atoms (Figure 1g).[19] To further reveal the oxidation state of the isolated Cu atoms in Cu@PCN, X-ray absorption near-edge structure (XANES) of Cu-foil, CuO and Cu@PCN are measured (Figure 1k). The absorption edge of

Cu@PCN is located between the Cu foil and CuO, indicating that the Cu atoms possess a slightly positive valence state loaded between 0 and +1. Subsequently, the extended X-ray absorption fine structure (EXAFS) is performed to observe the local coordination environment around the Cu sites. There is no Cu-Cu coordination within the Cu@PCN from the Fourier-transformed (FT) k^3-weighted EXAFS spectra (Figure 1l), distinctly underscoring the isolated feature of Cu atoms.[20] In addition, the EXAFS spectrum of *R* space for Cu@PCN discloses a dominated peak at approximately 1.43 Å ascribed to the coordination effect between Cu and N, also precluding the existence of Cu species as nanoparticles or clusters. According to the detailed fitting results of the EXAFS, Cu single atom sites are present in the configuration of CuN_3 (Figure 1m).[21] Wavelet transform (WT) was adopted to further investigate Cu K-edge EXAFS oscillations (Figure1n). Cu@PCN reflects intensity maximum at ≈ 4.1 $Å^{-1}$ in the k-space, which can be due to the Cu-N structure, while the intensity maximum corresponding to Cu–Cu is invisible. Therefore, it is confirmed that Cu is atomically dispersed based on the TEM, XRD and XAFS results. Moreover, the N_2-sorption isotherm reflects that the surface area of Cu@PCN is ≈ 66.5 $m^2\ g^{-1}$ (Figure S6, Supporting Information). A large specific surface area helps to expose more Cu single atomic active sites, beneficial to the faster diffusion of Zn^{2+}. The uniform and dense coating thickness of the Cu@PCN/PVDF powders is ≈ 11.5 μm, as estimated by the cross-sectional SEM image (Figure S7, Supporting Information). Furthermore, Cu@PCN-Zn fabrication is prepared using an appropriate amount of viscous PVDF (10 wt.%) to guarantee outstanding adhesion and mechanical robustness between the Cu@PCN and zinc plate after the bending and twisting tests (Figure S8, Supporting Information). Even after many times tests, the Cu@PCN coating still stays intact on the surface of zinc foil with no any visible cracks and peeling.

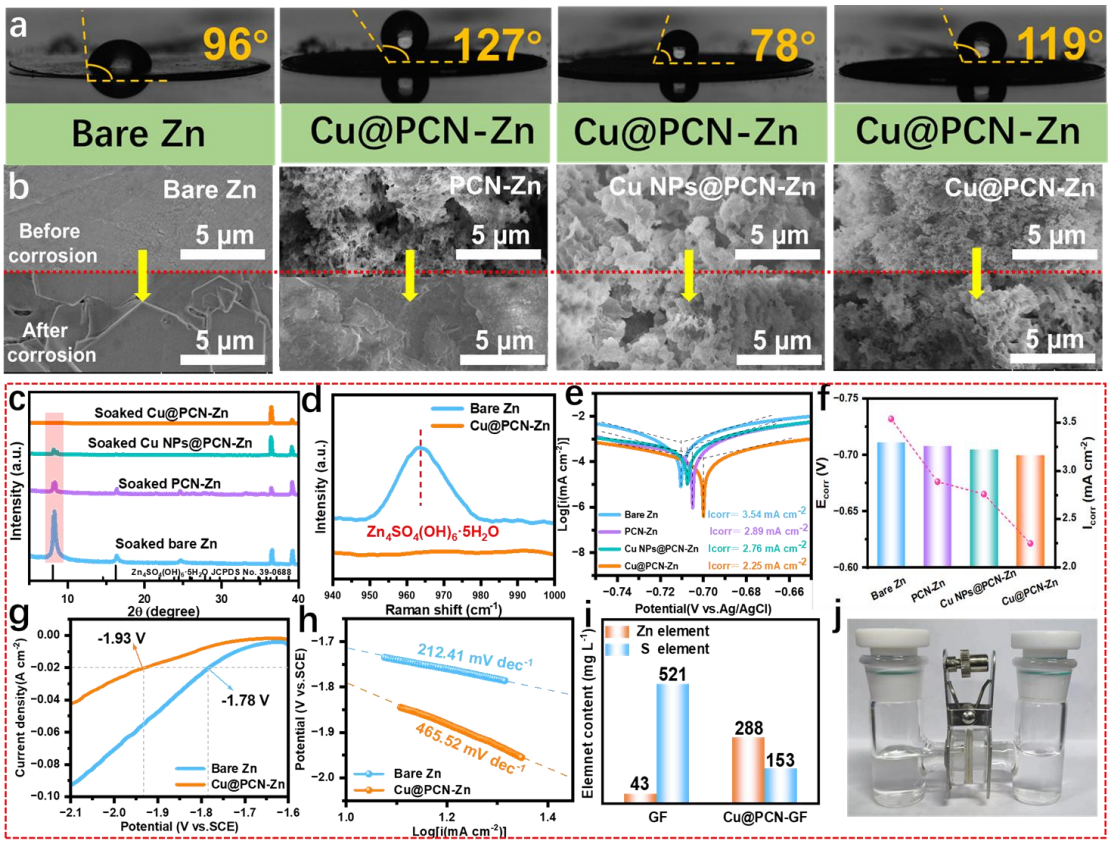

Figure 2. Side reaction resistance of Cu@PCN-Zn electrode. (a) images of contact angles of the 2 M $ZnSO_4$ on bare Zn foil, Cu@PCN-Zn, water wetted then dried Cu@PCN-Zn foil and 2 M $ZnSO_4$ wetted then dried Cu@PCN-Zn foil. (b) SEM images of different electrodes in the initial state and after immersion in 2 M $ZnSO_4$ electrolyte for 3 days. (c) XRD patterns and (d) Raman spectra of different electrodes after immersion. (e,f) Corrosion, (g) HER curves and (h) the corresponding Tafel slopes of different electrodes. (i) Zn^{2+} and SO_4^{2-} permeability of GF and Cu@PCN-GF membrane. (j) Diffusion experiments with Cu@PCN-GF separator in the H-cell.

The surface wettability is measured through the contact angle test for bare Zn, PCN-Zn, Cu NPs@PCN-Zn and Cu@PCN-Zn in 2 M $ZnSO_4$ electrolytes. As presented in Figure 2a and Figure S9， Supporting Information, the electrolyte on Cu@PCN-Zn performs a higher contact angle of 127° relative to that on pure Zn (96°) and PCN-Zn (118°), reflecting a more hydrophobic property on the surface of Cu@PCN. Although PVDF may possess a slight effect on hydrophobicity (115°), the hydrophobic surface of Cu@PCN-Zn reasonably ascribed to PCN-based materials can relieve the $ZnSO_4$ electrolyte from reaching and corroding the active zinc surface. It is noteworthy that the contact angle becomes 78° on the electrolyte-wetted-then-dried Cu@PCN-Zn, while a negligible change is maintained in the reference values for the

water-wetted-then-dried Cu@PCN-Zn (119°). Such a result can be assigned to the zincophile properties of $ZnSO_4$, and PCN-based materials due to large numbers of lone pair electrons from structural nitrogen and periodic coplanar pores.[22] Therefore, the hydrophobic Cu@PCN layer, acting as a protective shield, effectively prevents direct contact between the Zn anode and the electrolyte.

To verify the protective effect of the Cu@PCN coating for the Zn anode, the zinc anode with and without coatings (bare Zn, PCN-Zn, Cu NPs@PCN-Zn and Cu@PCN-Zn) are immersed into an aqueous electrolyte containing 2 M $ZnSO_4$ for 3 days. The bare Zn surface becomes dark and rough, devoid of its characteristic metallic luster after 3 days, while the surface of electrodes with Cu NPs@PCN-Zn and Cu@PCN-Zn can basically retain their initial appearance after 3 days and no discernible detachment nor fragmentation from the Zn foil are observed, revealing that the superior mechanical strength and chemical stability of the Cu@PCN coating (Figure S10， Supporting Information). Moreover, the corresponding SEM images after immersion are depicted in Figure 2b. Remarkably, numerous hexagonal flake-like crystals are clearly detected on the surface of pure Zn after immersing in electrolyte, while the surface of the Cu@PCN-Zn electrode still maintains the original morphology. Meanwhile, optical microscopy is also employed to obtain 3D height images after soaking (Figure S11， Supporting Information). The surface roughness parameters, such as R_a, R_z, and R_{zjis} are listed in Table S1, Supporting Information, to quantitatively represent the overall morphology and roughness of zinc sheet surfaces. The bare Zn electrode soaked in aqueous $ZnSO_4$ solution exhibits nonuniform and large zinc protrusions with R_a, R_z, and R_{zjis} of 7.3, 26.6, and 22.4 μm, respectively. In contrast, the surface of Cu@PCN-Zn is relatively flat and compact, maintaining low surface roughness (R_a: 1.2 μm, R_z: 4.9 μm, and R_{zjis}: 3.0 μm). From the XRD results (Figure 2c), the obvious diffraction peak at approximately 8.3° appear for the bare Zn, PCN-Zn and Cu NPs@PCN-Zn electrodes after the immersing test, which corresponds to the $Zn_4SO_4(OH)_6$•$5H_2O$ (JCPDS#39-0688) by-product formed on the Zn electrode surface,[23] indicating their poorer side reaction resistivity, whilst no obvious peaks of the side product are visible for Cu@PCN-Zn electrode. The Raman

spectrum for bare Zn after immersion in $ZnSO_4$ electrolyte presents a strong peak at 960 cm^{-1}, corresponding to the generation of $Zn_4SO_4(OH)_6 \bullet 5H_2O$,[24] whilst this peak is absent in the corresponding spectrum for Cu@PCN-Zn electrode (Figure 2d). Therefore, side reactions on the Zn surface can be alleviated by applying Cu@PCN coating.

Subsequently, the anticorrosion effect of the Cu@PCN on Zn foil is investigated through linear polarization measurements adopting a three-electrode system in 2 M $ZnSO_4$ electrolyte to further verify the excellent corrosion resistance (Figures 2e,f). It can be observed that the Cu@PCN-Zn performs a lesser corrosion current density (I_{corr}, 2.25 mA cm^{-2}) and a higher corrosion potential (E_{corr}, –0.702 V) than bare Zn (3.54 mA cm^{-2} and –0.713 V), PCN-Zn (2.89 mA cm^{-2} and –0.707 V) and Cu NPs@PCN-Zn (2.76 mA cm^{-2} and –0.708 V), which should be mainly benefited from effective suppression of side-reaction and acceleration of Zn^{2+} transport applying multifunctional Cu@PCN interface. Moreover, the developed interfacial host might possess a high HER overpotential originating from the hydrophobicity of Cu@PCN, thereby effectively restricting the interfacial side reactions. To illustrate the suppression of side reactions of Cu@PCN coating, the HER of bare Zn and Cu@PCN-Zn is analyzed by linear sweep voltammetry (LSV) employing 1 M Na_2SO_4 aqueous electrolyte due to competitive relationship between HER and zinc deposition. Without the interference of Zn ion redox reaction, the tested current density in the LSV profiles could accurately estimate the intensity of HER. As shown in Figure 2g, the Cu@PCN-Zn performs a smaller current density than those of bare Zn at a potential from −1.6 V to −2.1 V (vs Ag/AgCl). Additionally, the lower hydrogen evolution of Cu@PCN-Zn (−1.93 V) at the set potential delays the HER compared to those of bare Zn (−1.78 V), which can contribute to favorable zinc deposition while inhibiting the dynamic HER. Therefore, the suppression of the HER by Cu@PCN-Zn, diminishing OH^- generation (a major reason of side reactions), mitigates the maniacal zinc corrosion and by-products accumulation. And the corresponding Tafel slope fitted by LSV profiles for Cu@PCN-Zn electrode (465.52 mV dec^{-1}) is higher than that of the bare Zn (212.41 mV dec^{-1}) (Figure 2h), further

illustrating the sluggish HER tendency endowed by multifunctional Cu@PCN interface. At the same time, the corrosion rate of the Zn anode with and without coating is evaluated by monitoring the pH evolution during the cycle of symmetric cell (Figure S12, Supporting Information). As observed, there was no significant increase on the pH of the electrolyte in the presence of Cu@PCN during the cycle, in sharp contrast to the bare Zn foil displays a continuous rise for pH value due to the intimate contact of water, reflecting an excellent suppression ability of undesirable side reactions for the hydrophobic layer.

The Zn^{2+} transference number (t_{Zn}^{2+}) is calculated via the Bruce-Vincent method (Equation S1, Supporting Information) to further verify the contribution of the Cu@PCN layer to the transport facilitation capacity of Zn^{2+} (Figure S13, Supporting Information). Since the faster migration rate of anions than that of solvated Zn^{2+}, the t_{Zn}^{2+} in the bare Zn cell is calculated to be as low as 0.51, After introducing the Cu@PCN layer, the t_{Zn}^{2+} is improved to 0.75, reflecting the Cu@PCN layer can improve Zn^{2+} kinetics by capturing Zn^{2+} cations and repelling SO_4^{2-} anions. In order to further demonstrate the ability of Cu@PCN layer to isolate water solvent and transport Zn^{2+} ions, a diffusion experiment is performed using Cu@PCN-coated hydrophilic GF separator (Cu@PCN-GF) within a H-cell (Figures 2i,j). The experimental design consists of introducing 2 M $ZnSO_4$ electrolyte to the left side of the H-cell and deionized water (8 mL) to the right side. The ICP tests of the collected deionized water after 120 min of magnetic stirring reveal that the Zn content in the Cu@PCN-GF membrane is ≈1.88 times that of S, while pristine GF shows 12.11 times higher S content than that of Zn, further indicating that APL fabricated by Cu@PCN could significantly facilitate Zn^{2+} diffusion and limit SO_4^{2-} diffusion, which is beneficial to uniform Zn^{2+} distribution. As shown in Figure S14, Supporting Information, the Cu@PCN layer displays a high ionic conductivity of 2.04×10^{-3} S cm^{-1} (Equation S2, Supporting Information), manifesting the facilitated diffusion of Zn^{2+} ions.

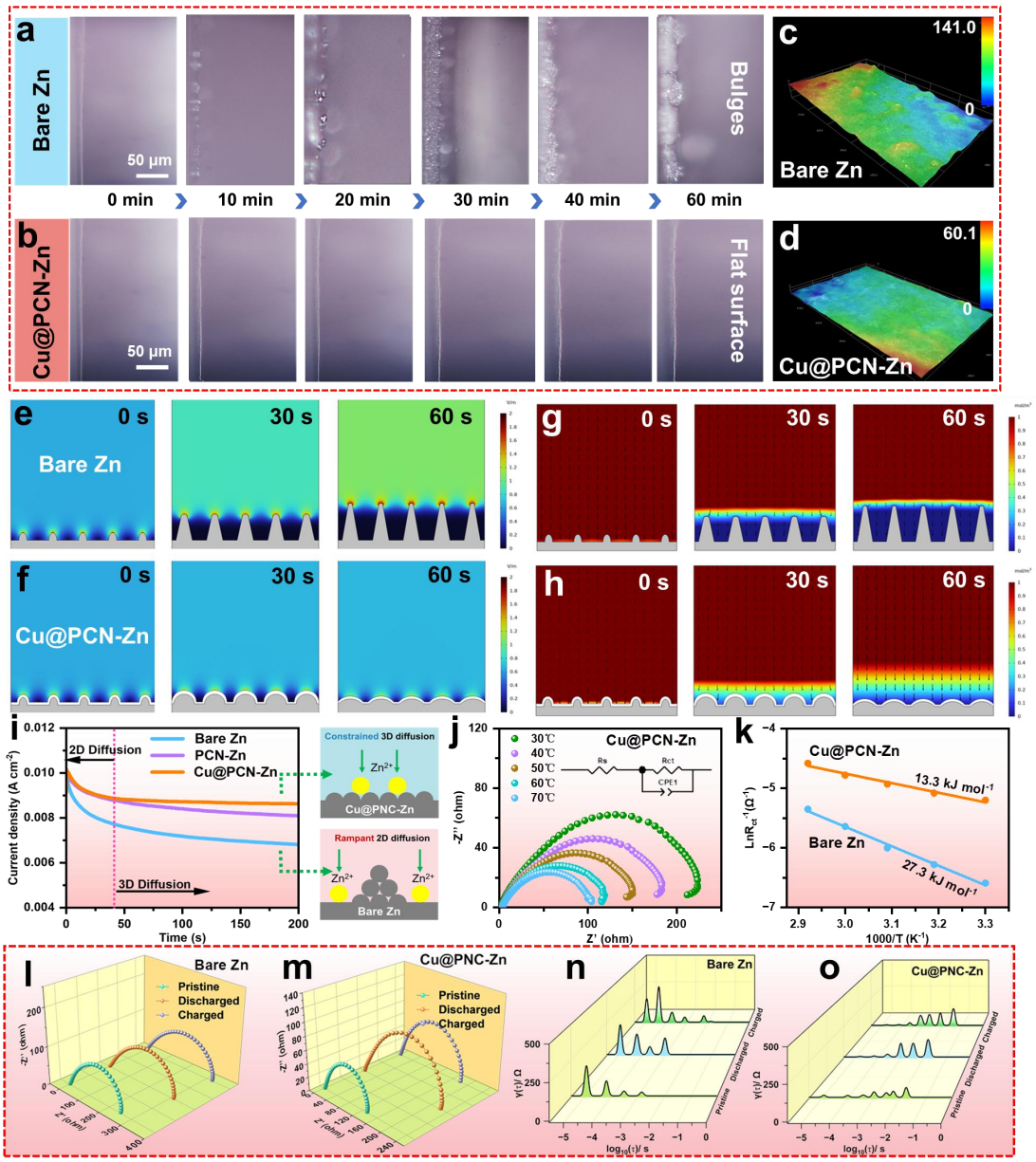

Figure 3. In situ optical microscope images of (a) bare Zn and (b) Cu@PCN-Zn anodes at 5 mA cm^{-2} and (c,d) the corresponding optical microscope images after 60 min. The numerical simulation of electric field distribution and equilibrium Zn^{2+} concentration at 0 s, 30 s, and 60 s under (e,g) bare Zn and (f,h) Cu@PCN-Zn. (i) CA tests of different electrodes at an overpotential of –150 mV. The EIS curves of (j) Cu@PCN-Zn symmetrical cell at different temperatures. Inset is the equivalent circuit. (k) The calculated desolvation activation energies of bare Zn and Cu@PCN-Zn electrodes. EIS curves of (l) bare Zn and (m) Cu@PCN-Zn cells during EIS measurements, and corresponding analysis of distribution of DRT upon galvanostatic in (n) bare Zn and (o) Cu@PCN-Zn, respectively.

To further unveil the function of the Cu@PCN layer, in situ optical microscopy was employed to directly visualize the real-time dynamic behavior of zinc plating at a set

current density of 5 mA cm^{-2}. As shown in Figure 3a, when the deposition time is 10 min, non-uniform nucleation of Zn^{2+} in bare Zn can be detected. As time progresses, this detrimental phenomenon becomes more serious. Especially after deposition for 60 min, the exposed zinc surface is covered with prominent Zn dendrites, exhibiting an extremely uneven surface. On the other hand, as the plating goes on, the thickness of deposited layer is almost negligible in the Cu@PCN-Zn, and a dense deposition morphology is visible on the electrode surface, which is ascribed to the denser and finer zinc core seed (Figure 3b). The 3D optical surface-profilometry images is also utilized to highlight height differences in plating uniformity. As depicted in Figure 3c, bare Zn foil reveals a large altitude intercept due to the rugged and loose surface with large amounts of protrusions and pits throughout the whole plating process. Comparatively, the Cu@PCN coating endows the Zn electrode with a large number of zinc nucleation sites for uniform plating and thus a flat and dense surface with relatively small height fluctuation due to the regulation of zinc deposition behavior of as presented in Figure 3d. Furthermore, finite element analysis is conducted applying the numerical simulation to demonstrate the charge polarization effect of Cu@PCN in manipulating the electric field. For Cu@PCN-Zn system, the atomically dispersed Cu-N_3 sites effectively regulates charge distribution and redistributes the electric field at Zn anode-electrolyte interphase. The width of the concentration polarization region shows significant stability throughout the Zn electroplating process (Figure 3h), and the current density distribution on the Zn surface remains uniform (Figure 3f). This is attributed to Cu-N_3 sites with excellent zincophilic properties ensures fast and adequate ion compensation on the concave. Conversely, bare zinc exhibits dendritic Zn deposits on its surface, resulting in an uneven concentration field. As Zn deposits progressed on bare zinc, the width of the concentration-polarized region with a lower Zn^{2+} concentration gradually increases. Evidently, the growth tips reveal a remarkably higher Zn^{2+} concentration than the valley region (Figure 3g), causing the cell failure. This differential Zn^{2+} accumulation, coupled with a non-uniform current density distribution, induces a “tip effect” favoring the growth of Zn dendrites (Figure 3e).

From the chronoamperometry (CA) test as presented in Figure 3i, the different Zn

deposition behaviors in the anodes with or without coating are reflected. Under an overpotential of –150 mV, the electrode with bare Zn produces a trend with continuous decrease for above 200 s, corresponding to the tedious and uncontrollable 2D diffusion deposition process of Zn^{2+}, which gives rise in the inhomogeneous deposition and the eventual dendrite propagation. The PCN-Zn electrode takes 142 s for 2D surface diffusion process before the current density becomes stable. For Cu@PCN-Zn system, however, it significantly shortens 2D diffusion time to 25 s and rapidly shifts to stable 3D diffusion mechanism, evidencing that a uniform distribution of Zn-ions with limited 2D ion migrate. Apart from to the above superiority, the Cu@PCN interphase is also expected to be conducive to the de-solvation effect of hydrated Zn^{2+}($[Zn(H_2O)_6]^{2+}$).[25] Hence, the Arrhenius activation energy (E_a) based on the Arrhenius formula (Equation S3, Supporting Information) is recorded to estimate the reaction kinetics of zinc plating over a temperature range from 303.15 to 243.15 K (Figure 3j and Figure S15, Supporting Information). More palpable impedance decreases for Zn anode in Cu@PCN-Zn than that in the bare Zn at different temperatures can be summarized in Table S2, Supporting Information. According to the relevant fitting results, the calculated E_a value of the Cu@PCN-Zn (13.3 kJ mol^{-1}) is much lower than that of the bare Zn (27.3 kJ mol^{-1}) (Figure 3k), meaning that the introduction of Cu@PCN as a superior interfacial agent enabled by the reducing energy consumption possesses a beneficial effect on eliminating the solvation sheath of Zn^{2+} and promoting the transfer kinetics of Zn^{2+}. For more in-depth investigation on the interfacial kinetics, the in-situ electrochemical impedance spectroscopy (EIS) of electrodes with and without the protective coatings are recorded (Figures 3l,m) and the corresponding EIS spectrum are deeply analyzed by the distribution of relaxation times (DRT) (Figures 3n,o). The peaks with relaxation time $\log_{10}(\tau)$ of between −4s and −1s are attributed to the charge transfer process of Zn-ions cross the interface.[26] Evidently, the value of R_{ct} in the cell with bare Zn increases greatly after plating/stripping, whereas the cell containing Cu@PCN-Zn maintains relatively constant, indicating a significant decrease of the byproducts. It is worth noting that Cu@PCN-Zn reveals a new peak at about −1s compared to bare Zn, which

mainly derives from the presence of artificial protective layers on Zn surfaces.

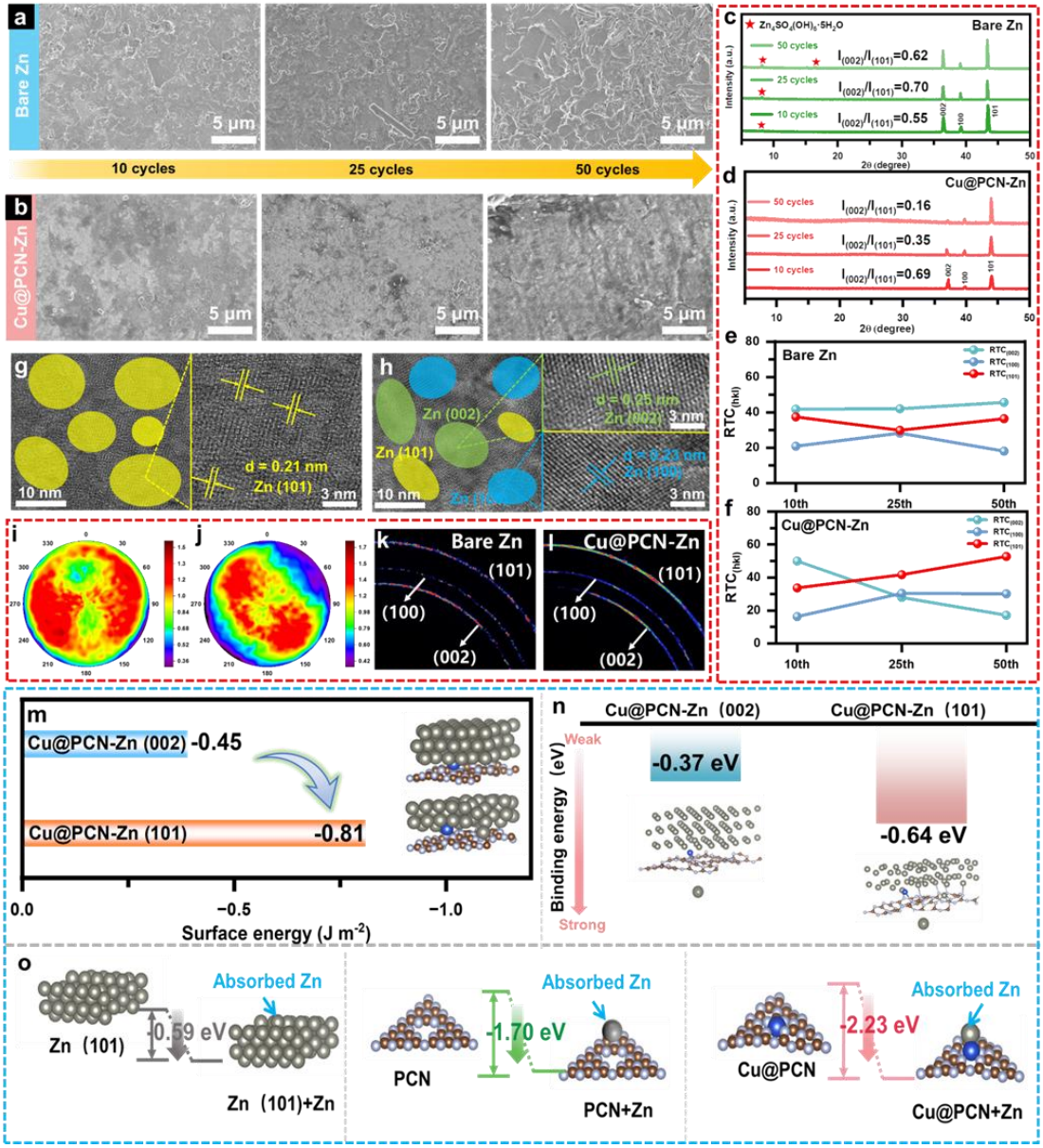

Figure 4. Analysis on the evolution of zinc deposition morphology and crystallographic texture of zinc surface. (a,b) The collected SEM images and (c,d) XRD patterns of the surface of zinc plate after different cycles for bare Zn and Cu@PCN-Zn electrodes. (e,f) The corresponding line chart for the fitted RTCs of Zn (002), Zn (100) and Zn (101) planes. The TEM images of Zn flakes after 50 cycles for (g) Cu@PCN-Zn and (h) bare Zn electrodes. The (101) pole figures of the Zn deposits in (i) bare Zn and (j) Cu@PCN-Zn at 5 mA cm^{-2} with a capacity of 1 mAh cm^{-2}. The 2D GIWAXS results of Zn anodes after 50 cycles in (k) bare Zn and (l) Cu@PCN-Zn at 5 mA cm^{-2} with a capacity of 1 mAh cm^{-2}. (m) The comparison of the Cu@PCN-Zn (101) and Cu@PCN-Zn (002) calculated surface energy. (n) The calculated binding energies between Zn atoms and Zn (101) and Zn (002) with Cu@PCN coating. (o) The binding energies of Zn (101), PCN and Cu@PCN to Zn atoms.

The morphology evolution of bare Zn anode and modified Zn anode electrodes at different cycles with a cutoff capacity of 1 mAh cm^{-2} at 1 mA cm^{-2} is firstly characterized by SEM (Figures 4a,b and Figure S16, Supporting Information). A rather disordered and irregular surface morphology with the generation of large amounts of randomly stacked zinc protrusions could be observed in post-cycling bare Zn electrode after only 10 cycles (Figure 4a), which may stem from the repeated and non-uniform zinc nucleation and Zn^{2+} stripping. As illustrated by SEM images in Figure S16a, Supporting Information, the surface of PCN-coated Zn anode remains flat and compact without dendrites formation during the cycling process, but after 50 cycles the hexagonal dendrites can be clearly found. Comparatively, the Cu@PCN coating enables the cycled Zn anode to perform a compact and dendrite-free deposition without visible pit and crack production during the cycling of the electrode (Figure 4b), consistent well with the significant enhancement in the electrochemical stability of the battery. The cross-sectional SEM and Optical microscope images shown in Figures S17, S18, and Table S3, Supporting Information further reflect this process. Moreover, the thickness of the Cu@PCN-Zn symmetric cell during cycling shows no significant change, whilst the dramatic increase in thickness of bare Zn demonstrates the severe HER (Figure S19, Supporting Information). The crystalline phase analysis by ex-situ XRD of Zn electrodes after different stripping/plating cycles could be used to further demonstrate oriented dense zinc deposition pattern with the assistance of Cu single atoms. In detail, the intensity ratio (R= I_{002}/I_{101}) of Zn (002) and Zn (101) is used to determine the orientation of the zinc deposition. As shown in Figures 4c,d, comparing with bare Zn and Cu@PCN-Zn anode, the R value of $I_{(002)}/I_{(101)}$ dramatically decreases to 0.16 for Cu@PCN-Zn electrode after 50 cycles, while R value increases to 0.62 for bare Zn under the same circumstances, suggesting the oriented dense zinc deposition along Zn (101) facet modulated by Cu@PCN coating. For further characterizing the crystallographic orientation of the Zn anode, as one of the most significant indexes, the relative texture coefficient (RTC) for three typical crystal planes is calculated based on the following formula: $RTC_{(hkl)}$ =

$\frac{I_{(hkl)}/I_{0(hkl)}}{\sum(I_{(hkl)}/I_{0(hkl)})} \times 100$. A larger RTC value means a more obvious the texture.[27] Consequently, according to the XRD patterns, the RTC diagrams of different crystal planes versus cycles for pure Zn and Cu@PCN-Zn electrodes are further illustrated. As shown in Figure 4e, the RTCs acquired respectively pointing to Zn (002), Zn (101), and Zn (100) planes of the zinc electrode after different cycles in the bare Zn system show irregular variations, revealing the absence of preferential crystal orientation for any Zn planes during the cycle. On the contrary, Zn (101) plane of the Cu@PCN-Zn harvests a significant improvement as the cycle deepened, whereas that of Zn (002) plane dramatically decreases. Specifically, the RTC of the Zn (101) plane rapidly rise from 33.7 to 52.8 after 50 cycles, while that of Zn (002) plane significantly decline from 50.0 to 17.1 at the same time (Figure 4f). The result of the RTC greatly supports Cu@PCN-Zn system could realize the manipulation of crystal orientation and oriented dense deposition by inducing preferential exposure of Zn (101) crystal plane rather than Zn (002) plane, thus enabling the uniform and dendrite-free Zn plating. Besides, the several peaks involving irreversible production of $Zn_4SO_4(OH)_6 \cdot 5H_2O$ on bare Zn anode are clearly observed, which suffers from corrosion passivation of zinc metals. On the contrary, the Cu@PCN-Zn electrode shows nearly the same diffraction peaks as the initial state, further indicating this APL could mitigate dendrite formation by inducing oriented dense Zn deposition. The different Zn crystal plane orientation types are analyzed using high-resolution TEM characterization with bare Zn and Cu@PCN-Zn (after 50 cycles), and it was clear that no other impurities are observed on the modified-Zn surface except for the newly deposited surface with an interplanar distance of 0.21nm, which could be labeled as the Zn (101) surface (Figure 4g and magnified views). Conversely, the TEM image of Zn flakes cycling in the bare system reveal disordered crystal planes, which can be ascribed to the uncontrolled nucleation and deposits of Zn atoms (Figure 4h and magnified views), again confirming the occurrence of a dense oriented deposition behavior on Zn electrode during cycling by multi-interface regulation. Furthermore, the texture details of the Zn deposits are also characterized adopting X-ray diffraction pole figures and 2D GIWAXS patterns. As

depicted in Figure 4j, the (101) pole of Zn with Cu@PCN coating reflects a sharp intensity concentration suggesting a texture structure of the zinc platelets along the (101) direction. In contrast, an arbitrary distribution of bare Zn deposits would cause a wide range of grain orientations (Figure 4i). This induces the (101) pole figure to exhibit a broad image of the diffraction intensity, indicating a less textured orientation along (101). As shown in 2D GIWAXS patterns (Figures 4k,l), Cu@PCN layer greatly changes the texture of the deposited zinc. In these patterns, three Debye rings appear clearly, representing the (002), (100) and (101) crystal planes, respectively. For Cu@PCN-Zn, the diffraction intensity of the (101) crystal plane is the highest, suggesting a pronounced preference for the (101) crystal plane orientation. Conversely, in the case of bare zinc, the luminance of the (101) planes are dispersed and inconspicuous, signifying the deposited layer is disorderedly oriented.

To elucidate the underlying mechanism dictating the modulation of Zn electroplating crystallinity and morphology by Cu@PCN, the surface energy is conducted employing density functional theory (DFT) calculations (Figure 4m). The Cu@PCN-Zn (101) has a lower surface energy (–0.81 J m^{-2}) than that of the Cu@PCN-Zn (002) (–0.40 J m^{-2}), implying that the Zn (101) plane with Cu@PCN has a stronger binding affinity for Zn atoms. This stronger affinity can lead to more uniform deposition of Zn on the Zn (101) plane, as it presents a surface that is more energetically favorable for Zn nucleation and growth, which infers that the Zn (101) plane tends to be preferentially exposed during the zinc nucleation stage on the basis of crystal growth theory and can supply a substrate for homoepitaxial growth in the subsequent cycling. As previously analyzed, Cu@PCN can significantly promote Zn^{2+} migration kinetics, combined with further reduced surface energy for Zn (101), thus preferential orientation of zinc deposits along (101) becomes available. The Zn (101) plane can offer more favorable pathways for Zn^{2+} ion transport and reduced resistance to ion migration, which contribute to better cycling stability and higher CE for zinc-ion batteries. As shown in Figure 4n, the binding energy of Zn atoms and Zn (101) with Cu@PCN exhibits a value of –0.64 eV, of great competitive than that of Zn (002) with Cu@PCN (–0.37 eV), further demonstrating the affinity between Zn atoms and

Zn (101) with Cu@PCN coating. The coating could adjust the electronic structure of the surface, improving the adsorption characteristics of Zn atoms on the Zn (101) plane. This optimization can reduce energy barriers during deposition, making it easier for Zn atoms to form stable chemical bonds on the Zn (101) plane. The interactions between the Zn^{2+} and different sites in Cu@PCN are further estimated by DFT. As demonstrated in Figure 4o, the binding energies of Zn ion on Cu@PCN (–2.23 eV) is more negative than that on bare Zn (–0.59 eV) and PCN (–1.70 eV), suggesting that a lower energy barrier and higher selectivity of adsorption for Zn on the Cu@PCN. According to XPS analysis, Cu single atom is coordinated by nitrogen molecule (Cu-N_3 site). The excellent Zn affinity of the Cu-N_3 sites can effectively accelerate nucleation and deposition kinetics. As shown in Figure S20, Supporting Information, DFT calculations indicate that the adsorption energy of water molecules to Cu@PCN is –0.95 eV. It has been reported that the adsorption energies of water molecules to Zn^{2+} is –0.23 eV,[28] meaning that Cu@PCN possesses exceptionally strong interactions with the H_2O molecules in solvated Zn^{2+}. As a result, Cu@PCN coating could facilitate the $[Zn(H_2O)_6]^{2+}$ penetration and then trap the H_2O molecules by hydrogen bonds thus allowing direct reduction of Zn^{2+} on the metal substrate.

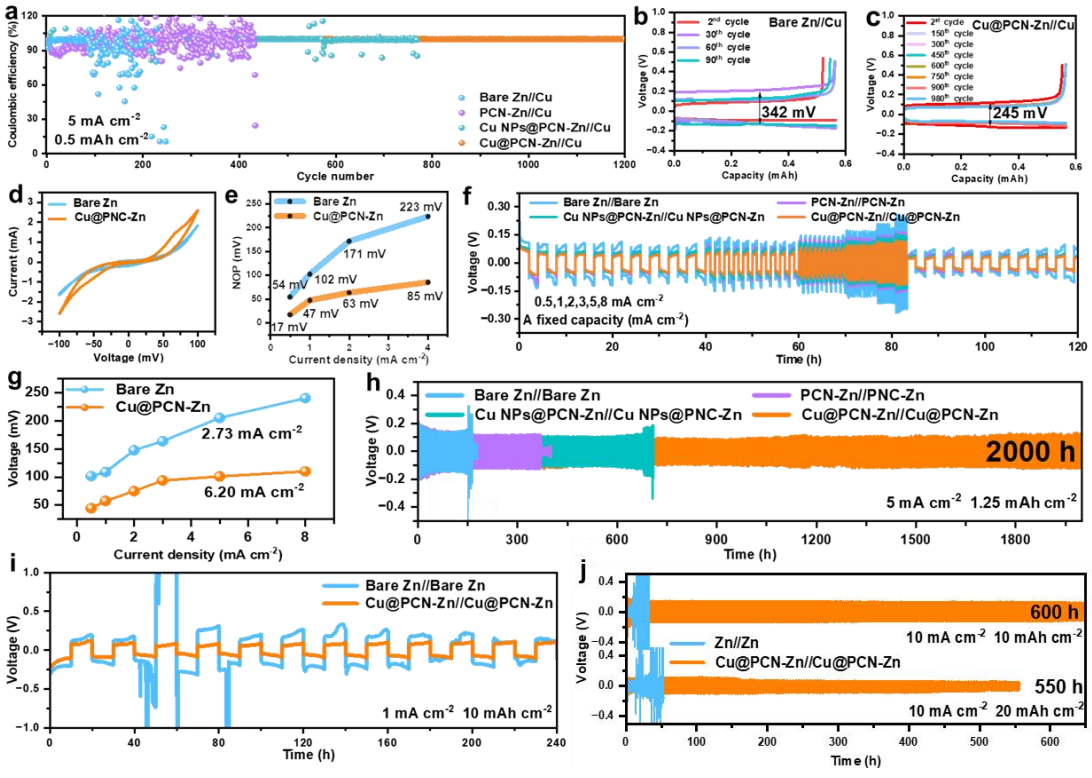

Figure 5. The electrochemical performance of symmetric and asymmetric cells. (a) CE profiles of the asymmetrical cells assembled by different electrodes at 5 mA cm^{-2}/0.5 mAh cm^{-2}, and the corresponding galvanostatic cycling curves for (b) bare Zn//Cu and (c) Cu@PCN-Zn//Cu asymmetry cells at different cycles. (d) CV curves of symmetric cells using bare Zn and Cu@PCN-Zn at a scan rate of 1.0 mV s^{-1}. (e) NOPs of zinc deposition on bare Zn and Cu@PCN-Zn at different current densities. (f) Rate performance of symmetric cells at current densities from 0.5 to 8 mA cm^{-2} with a fixed capacity of 1 mAh cm^{-2} and (g) corresponding exchange current densities of bare Zn and Cu@PCN-Zn. Long-term galvanostatic cycling performance of symmetric cells at current densities/capacities of (h) 5 mA cm^{-2}/1.25 mAh cm^{-2}, (i) 1 mA cm^{-2}/10 mAh cm^{-2}, and (j) 10 mA cm^{-2}/10 mAh cm^{-2}, 10 mA cm^{-2}/20 mAh cm^{-2}.

To demonstrate the advantages of Cu@PCN coating for Zn plating and striping, the Coulombic efficiency (CE) and cycle stability are investigated using Zn//Cu asymmetric and Zn//Zn symmetric cells, respectively. The CE of the asymmetric cell configuration (bare Zn//Cu, PCN-Zn//Cu, Cu NPs@PCN-Zn//Cu and Cu@PCN-Zn//Cu cells) is firstly quantified at a current density of 5 mA cm^{-2} with Zn plating capacity of 0.5 mAh cm^{-2}. (Figure 5a). After ≈ 80 cycles, the CE of the bare Zn//Cu cell suffers from obvious fading, which is springing from the gradual formation of "dead zinc" and short circuits due to serious side reactions and dendrite growth, whereas the CE of the Cu@PCN-Zn//Cu half-cell stays stable for 1200 cycles (1200 h) with a high average CE of ≈ 99.7%. Meanwhile, the CEs for the PCN-Zn//Cu and Cu NPs@PCN-Zn//Cu cell fluctuate violently after 100 cycles and 540 cycles, respectively, and then rapidly fails. The corresponding capacity-voltage curves at various cycles show a lower and more stable voltage gap for Cu@PCN-Zn//Cu (≈245 mV) compared to bare Zn (≈342 mV) (Figures 5b,c and Figure S21, Supporting Information). As shown in Figure S22, Supporting Information, the initial nucleation overpotential of the Cu@PCN-Zn is 30 mV, much lower than those of bare Zn (83 mV)， PCN-Zn (57 mV) and Cu NPs@PCN-Zn (42 mV), supporting the smallest polarization and highly efficient kinetics. Similarly, cyclic voltammetry (CV) profiles also lead to the same conclusion (Figure S23, Supporting Information). Interestingly, the shortest delay in the cathodic current (|AB| (25 mV) < |AB'| (56 mV)) is observed, which indicates that Cu@PCN can cause a lower nucleation overpotential of zinc deposition than bare Zn. To well clarify the acceleration of ion transport using

Cu@PCN layer, the EIS of four symmetric cells is conducted in Figure S24, Supporting Information. Obviously, the symmetric cell employing the bare Zn delivers a large charge transfer resistance (R_{ct}) of 1220 Ω, while the Cu NPs@PCN coating greatly diminishes this value to 280 Ω. Additionally, the Cu@PCN coating enables the value to further decrease to 135 Ω, which is ascribed to the improved zinc-affinity and decreased diffusion energy of Zn springing from the modification of Cu atoms, and implies faster charge transfer and zinc plating/stripping kinetics. CV experiments in symmetric cells are further performed to investigate reversibility and electrochemical kinetics of unmodified Zn and Cu@PCN-Zn during the plating/stripping (Figure 5d and Figure S25, Supporting Information). Compared with unmodified Zn, a larger peak area and higher maximum current density are obtained for Cu@PCN-Zn cell. This reflects the boosted electrochemical redox kinetics for zinc deposition and the elevated Zn^{2+} concentration on the Cu@PCN surface resulting from the abundant zincophilic nucleation sites, which contribute to uniform Zn deposition with a rapid Zn^{2+} transfer rate. Meanwhile, the CV curves of Cu@PCN-Zn after repetitive CV scanning almost overlap and possess identical shapes in contrast to the varying curves for bare Zn, again indicating the highly reversible zinc deposition/dissolution of Cu@PCN-Zn. In addition to enhancing the dynamics and reversibility of zinc deposition/dissolution, Cu@PCN coating also plays a crucial role in reducing zinc nucleation overpotential (NOP: the difference between voltage drop and the stable voltage plateau) values. As shown in Figure 5e and Figure S26, Supporting Information, the NOP of Cu@PCN-Zn at a current density of 0.5 mA cm^{-2} is 17 mV, much lower than that of bare Zn (54 mV), reflecting the smallest polarization and highly efficient kinetics. When the current density increases to 1, 2, and 4 mA cm^{-2}， respectively, the zinc growth overpotential of Cu@PCN-Zn (47, 63 and 85 mV) is always lower than that of bare Zn. The low deposition overpotentials reflect that Cu@PCN coating can strongly decrease the nucleation energy barrier and facilitate homogenous Zn deposition. The rate performance of symmetric cells is electrochemically verified at different current densities ranging from 0.5 to 8 mA cm^{-2}, each with a capacity of 1 mAh cm^{-2} (Figure 5f and Figure S27, Supporting

Information). Among the four symmetric cells, the cell with Cu@PCN-Zn always presents the best rate performance with lowest hysteresis and most stable Zn deposition/dissolution voltage curves during the whole examination. Even at a high rate of 8 mA cm^{-2}, the cell delivers a much-decreased polarization voltage of 110.1 mV, compared with that of bare Zn-based (240.3 mV), and PCN-Zn-based (160.3 mV), and Cu NPs@PCN-Zn-based (156.5 mV) cells. To accurately quantify the kinetics of zinc deposition, the exchange current density (i_0) is calculated adopting the Butler-Volmer approximation equation (Equation S4, Supporting Information) based on rate performance testing. As shown in Figure 5g, a higher i_0 of 6.20 mA cm^{-2} is achieved for Cu@PCN-Zn, which is approximately twice that of the cell with bare Zn (2.73 mA cm^{-2}). The improved zinc deposition kinetics of Cu@PCN-Zn underpin the effective enhancement of Zn deposition/dissolution behavior by Cu@PCN coating.

Additionally, cycling stability is assessed to further reveal the superiority of Cu@PCN layer for stabilizing Zn anode at different current densities/areal capacities. As expected, the symmetric decorated with the Cu@PCN layer is capable of stable and reversible voltage profile for over 1860 h at 1 mA cm^{-2} with a cycling capacity of 0.25 mAh cm^{-2}, which presents a regular fluctuations and more stable voltage hysteresis of around 76.3 mV (Figure S28, Supporting Information). On the contrary, the significant voltage fluctuations appear in the Cu NPs@PCN-Zn anode after ≈1000 h cycling. However, the symmetric cell employing the bare Zn and PCN-Zn display an abrupt failure at ≈155 h and ≈370 h, respectively, as a result of the dendrite-induced internal short circuit. Increasing the current density and the areal capacity of Zn plating/stripping will cause the non-uniform electric field at the anode/electrolyte interface, enlarge the dendrite size, and induce the formation of rampant dendrite. At the elevated current density/areal capacity of 5 mA cm^{-2}/1.25 mAh cm^{-2}, impressively, the Cu@PCN-Zn anode displays a thirteen-fold improvement in cycle life (2000 h) without the occurrence of violent voltage fluctuations or short circuits, outperforming to the cells with other Zn anodes, which show varying degrees of serious voltage fluctuation and polarization (Figures 5h and Figure S29, Supporting Information). Remarkably, a more demanding measurement is implemented at 10 mA cm^{-2}/10 mAh

cm^{-2} (Figure 5j and Figure S30a, Supporting Information). Similarly, the cell based on Zn foil fails to operate merely after 12 h of continuous cycling, whereas the Zn//Zn symmetric cell applying Cu@PCN coating depicts an extended lifespan of 600 h with superior voltage stability, approximately 50 times longer than the bare Zn. The same results can be acquired at current densities/capacities of 10 mA cm^{-2}/20 mAh cm^{-2} (Figure 5j and Figure S30b, Supporting Information). In practical applications, Zn anodes typically face more severe corrosion and HER at lower current densities, which are more relevant for real-world battery performance. Therefore, the Zn//Zn symmetric cells at lower current densities is carry out to meet practical applications in Zn-ion batteries. Benefiting from the advantage of highly dendrite-resistant Zn (101), the Cu@PCN-Zn system could still exhibit stable cycling for 240 h under the condition of 1 mA cm^{-2} and 10 mAh cm^{-2} (Figure 5i and Figure S31, Supporting Information). In comparison, the bare Zn//Zn symmetric cells quickly fail after merely 40 h, with dramatically fluctuating voltage curves observed. The soft shorts essentially boost the detrimental electrical conductivity and prevents the desired interfacial reactions in the battery. Based on this fact, herein, this issue with extra EIS and/temperature response tests is scrutinized to distinguish the possible soft shorts that easily lead to deceptive ultrastability. As a validation, Figures S31b–d, Supporting Information show that a significant decrease in the R_{ct} of Cu@PCN-Zn symmetric cell under 1 mA cm^{-2}/10 mAh cm^{-2}, which further decreases to a moderate value after 120 h. The whole process reflects no sudden drop in the R_{ct}, indicating that no soft shorts occur. Furthermore, an in-situ temperature response test is conducted to examine the issue in detail. The symmetrical cell including Cu@PCN-Zn after the long-term cycling harvests an increased voltage gap under lower temperatures, producing a positive E_a for the dynamic stripping/plating process (Figures S32, Supporting Information). This positive E_a is consistent with ion conduction characteristics (otherwise the electron conduction mechanism would produce negative E_a), thus corroborating a truly stable interfacial reaction generated on the modified zinc anode, rather than forming a soft short. The significant improvement in the electrochemical stability of the electrode at 1 mA cm^{-2}/10 mAh cm^{-2} is also characterized by ex-situ

SEM, XRD and XPS images after cycling (Figures S33–36, Supporting Information). The surface of bare Zn electrode after cycling becomes rather fragile and rough with the generation of numerous randomly stacked zinc protrusions as a result of the repeated and uneven Zn nucleation and Zn^{2+} stripping. Instead, the Cu@PCN coating makes the cycled Zn electrode to perform a flat surface without obvious byproducts and dendrite formation after cycling due to a dense oriented deposition along Zn (101) plane. The XRD and XPS results are consistent well with SEM results. Compared with previously reported works about modified Zn anodes, our work is outstandingly competitive in terms of the cumulative capacity (Figure S37 and Table S4, Supporting Information).

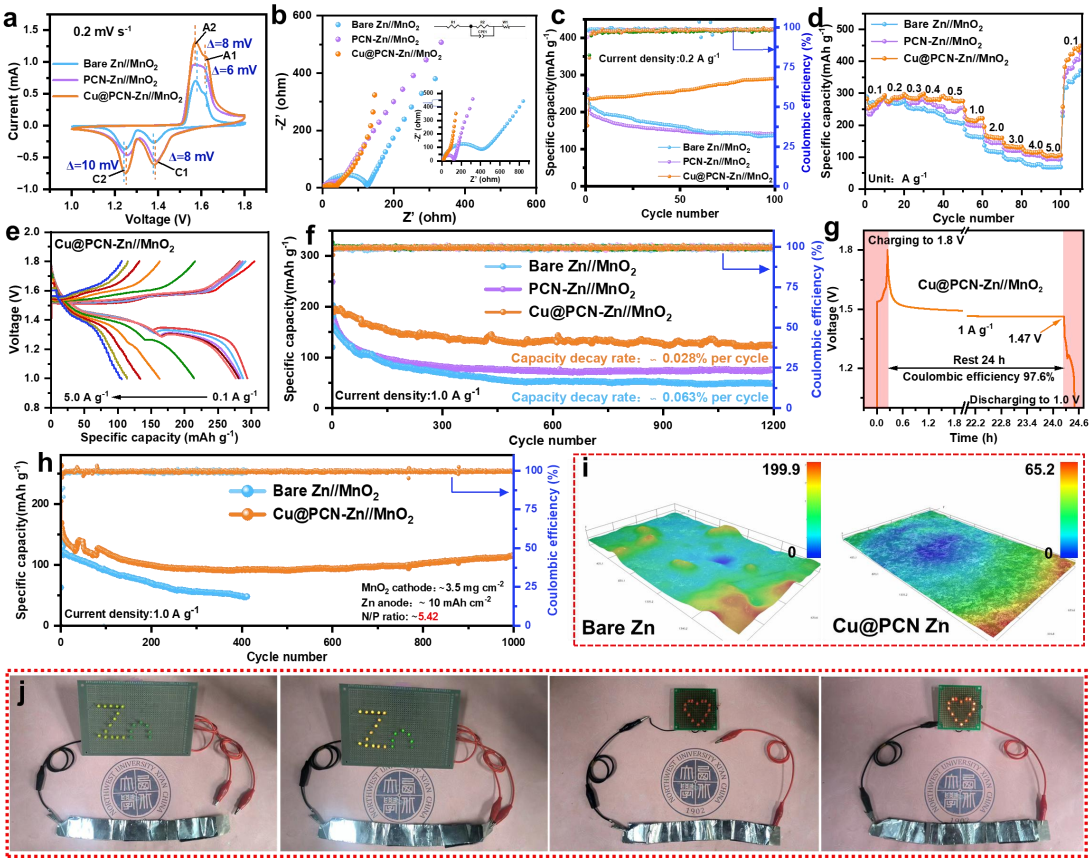

Figure 6. The electrochemical performance investigation of aqueous Zn//MnO_2 batteries. (a) CV curves at 0.1 mV s^{-1}, (b) EIS plots, (c) cycling stability at 0.2 A g^{-1}, (d) Rate performance and the corresponding long-term cyclic discharge voltage curves of (e) Cu@PCN-Zn//MnO_2 at various cycles. (f) Long-term cycling performance at 1 A g^{-1} of different full cells. (g) Self-discharge test of the Cu@PCN-Zn//MnO_2. (h) Cycling performance under restricted N/P ratio (≈5.42) at 1 A g^{-1}, and (i) the corresponding optical microscope images of bare Zn//MnO_2 and Cu@PCN-Zn//MnO_2. (j) A picture of three-connected cells lighting up an LED light.

Besides, the α-MnO_2 as cathode material is also applied in Zn-ion full cells for evaluation, whose XRD patterns and SEM images are exhibited in Figure S38, Supporting Information. After assembly of the Zn//MnO_2, PCN-Zn//MnO_2 and Cu@PCN-Zn//MnO_2 full cells, various electrochemical measurements are performed to compare the differences among the three cells. The CV profiles in the 1.0−1.8 V (*vs.* Zn^{2+}/Zn) at a sweeping rate of 0.2 mV s^{-1} depict that the three cells present two typical pairs of anodic/catholic peaks with high electrochemical reversibility (Figure 6a and Figure S39, Supporting Information), which correspond to H^+ and Zn^{2+} insertion/extraction into/from the α-MnO_2.[29] Moreover, the CV curves of three cells are almost identical, signifying that no other side reactions are introduced by the Cu@PCN layer. Obviously, the Cu@PCN-Zn//MnO_2 cell also delivers higher peak current density and smaller voltage polarization between redox peaks than the bare Zn full-cell, reflecting the higher capacity and electrochemical reactivity. Furthermore, the Nyquist plots of the full-cells before cycling (Figure 6b) distinctly show the boosted charge transfer and Zn^{2+} diffusion through a significantly reduced R_{ct} (33 Ω) for the Cu@PCN-Zn cell compared to the bare Zn cell (R_{ct}: 132 Ω). The Cu@PCN-Zn full-cell after 100 cycles still delivers low electrochemical resistance and high Zn^{2+} ion diffusion in comparison with bare Zn full-cell. These results suggest that Cu@PCN coating effectively improves electrochemical kinetics, even in the MnO_2 full-battery, which is in accordance with its smaller polarization. According to the equation: $i(V) = av^b$, where a and b are adjustable constants, and i and v are peak current and scan rate. When the b value is around 0.5, the charge–discharge process is controlled by diffusion behavior, while the b value of 1.0 indicates that the surface-controlled response is leading.[30] Here, the calculated b values of peaks 1, 2, 3, and 4 for the cells with Cu@PCN-Zn are 0.53, 0.55, 0.72, and 0.51, respectively, which are larger than that of the bare Zn (Figure S40, Supporting Information), proving that the surface-controlled process is boosted by Cu@PCN coating. To quantitatively estimate the Zn^{2+} diffusivity of the full-batteries, the CV tests at different scan rates are conducted to calculate the Zn^{2+} diffusion coefficients ($D_{Zn^{2+}}$) according to the Randles–Sevcik equation (Equation S5, Supporting Information). As shown in Figure

S41, Supporting Information, the D_{Zn}^{2+} of the Cu@PCN-Zn full-cell is higher than that of the bare Zn full cell in all cathodic and anodic reactions, leading to the redistribution of Zn^{2+} flux and simultaneously enables Zn^{2+} transport faster.

Cycling performance during reversible charging/discharging tests at a multiplicity of 0.2 A g^{-1} were further taken into consideration (Figure 6c), the Cu@PCN-Zn//MnO_2 cell displays more excellent cycling performance with a high capacity of 324.8 mAh g^{-1} after 200 cycles. The capacity increase with the increase of cycles, especially at a low current density, mainly originates from the deposition of Mn^{2+} onto the surface of the cathode to form MnO_x.[31] However, pristine Zn based full-cell is greatly decreased from the initial capacity of 245.8 mAh g^{-1} to 131.8 mAh g^{-1}. At a higher current density of 0.5 A g^{-1} (Figure S42, Supporting Information), Cu@PCN-Zn//MnO_2 cell can exhibit a discharge capacity of 187.3 mAh g^{-1} after 500 cycles with the capacity retention of 76.0%, compared with the capacity of 111.2 mAh g^{-1} with the capacity retention of 54.6% for pure Zn//MnO_2 system. Supportive evidence is also observed at rate capability for the cells with or without coatings at a wide range of 0.1 to 5 A g^{-1}(Figures 6d,e and Figure S43, Supporting Information). The full cell with Cu@PCN-Zn//MnO_2 consistently shows an enhanced discharge capacity compared to those of the other batteries at every current density. Even at 5 A g^{-1}, a high capacity of 105.9 mAh g^{-1} is achieved. When the rate returns to 0.1 A g^{-1}, Cu@PCN-Zn//MnO_2 harvests a capacity of 382.8 mAh g^{-1} with more than 100% capacity retention due to the gradual activation of the electrode. The superior rate performance of Cu@PCN full cell is attributed to the improvement of the zinc deposition kinetics and Zn^{2+} diffusivity on the anode side. The corresponding charge–discharge profiles at different current densities further support the excellent charging and discharging property of Cu@PCN-Zn//MnO_2 cell. Furthermore, a discharge capacity of 123.8 mAh g^{-1} and a remarkable CE of 99.8% are achieved by Cu@PCN-Zn//MnO_2 cell even after 1200 cycles at 1 A g^{-1} (Figure 6f), which is superior to those of bare Zn//MnO_2 and PCN-Zn//MnO_2 cells, with specific capacities of 49.5 and 75.3 mAh g^{-1}. Obviously, the capacities of these cells sharply drop in the initial 300 cycles, which is related to the dissolution of Mn^{2+} from the cathode. After 300 cycles, the

capacity of the Cu@PCN-Zn//MnO_2 can operate steadily until it undergoes 1200 cycles, while the capacity of the cell operated in others continues to decline. This is ascribed to inhibited Zn dendrites growth by improving the Zn plating/stripping stability for Cu@PCN-Zn//MnO_2 cell. The SEM images after cycling further explains concrete illustration. From the morphologies after cycling, obvious corrosion and conspicuous Zn dendrites are found on the surface of the bare Zn anode, while the surface of the zinc anode with Cu@PCN coating remains relatively flat and smooth without corrosion after 100 cycles at 1 A g^{-1} (Figures S44–47, Supporting Information). Due to the protective effect of the Cu@PCN coating, the occurrence of side reactions including dendrites, by-products and corrosion of the anode surface is reduced. In addition, the XRD tests and ex situ 3D optical microscope images further demonstrate the benefits for the cell with Cu@PCN-Zn//MnO_2 (Figures S48 and S49, Supporting Information). From these results, it is clear that a rationally designed APLs contributes to the practical application of long-life zinc ion batteries for energy storage devices.

Furthermore, the ability of Cu@PCN-Zn to greatly retards water-induced side reactions during long-time MnO_2 cell resting is verified by monitoring the self-discharge behavior resulting from the irreversible consumption of the electrolyte and zinc corrosion during the rest phase after full charging of full-cells. For this test, the bare Zn and Cu@PCN-Zn full-cells are fully charged to 1.8 V at 1 A g^{-1} and then discharged to 1.0 V after resting for 24 h. As seen in Figure 6g and Figure S50, Supporting Information, the Cu@PCN-Zn full-cell presents a highly suppressed self-discharge behavior with a slight capacity loss of ≈ 2.4%, whereas the pure Zn full-cell retains merely ≈ 85.6% of the original capacity, signifying that the effective suppression of interfacial side reactions is well demonstrated in the full-cell with Cu@PCN-Zn. Most studies on AZIBs typically use excess Zn (thickness: ≥100 μm, capacity: ≥58.55 mAh cm^{-2}) and low loading MnO_2 cathodes (≤2 mg cm^{-2}). Such cells are far from being used in practical applications resulting from their rational ratio of negative electrode to positive electrode (known as N/P ratio), which restricts the energy density of AZIBs.[32] Thus, to evaluate AZIBs for rigorously practical

application, the long-term cycling performance of full cells under high Zn anode utilization (high loading cathode, limited zinc supply, low N/P ratio) are constructed. As displayed in Figure 6h, the Cu@PCN-Zn//MnO_2 cell with a limited N/P ratio of 5.42 can still harvest a discharge capacity of 110.7 mAh g^{-1} after 1000 cycles accompanied with an average CE of 99.5% at 1 A g^{-1}, while the discharge capacities of the bare Zn//MnO_2 cell deteriorates sharply after 412 cycles. The surface morphology of the bare Zn and Cu@PCN-Zn anodes after cycling are revealed by optical microscope images (Figure 6i). The bare Zn electrodes show sharp height fluctuations and a high-altitude intercept of 102 μm, attributing to the uncontrolled growth of Zn dendrites. However, the surface of Cu@PCN-Zn electrode is relatively smooth with a low altitude intercept of only ≈57 μm after cycling. Demonstratively, the Zn//MnO_2 cells assembled with Cu@PCN could comfortably power a series of LEDs (Figure 6j), verifying their practical applicability.

3. Conclusion

In conclusion, a multifunctional interface modification Cu@PCN layer was achieved to simultaneously greatly mitigate the undesirable HER and harmful parasitic reactions as well as the production of irreversible by-products on the surface of zinc anode. Experimental results and theoretical calculations suggest that atomically dispersed, high reversible Cu-N_3 zincophilic sites through coordination engineering with strong Zn^{2+} adsorption as well as strong charge polarization effect can regulate redistribution for local space electric field, enables a decrease in the nucleation overpotential and guarantee the even Zn nucleation under a nano-level. The hydrophobic and zincophilic Cu@PCN layer can effectively relieve the side reactions by isolating the zinc anode from the aqueous electrolyte and promote homogeneous zinc deposition in the plating/stripping process. At the same time, the Cu@PCN coating decreases the surface energy of the highly dendrite-resistant Zn (101) plane, thus boosting oriented and continuous phase epitaxy towards the Zn (101) crystal plane. Benefitting from such oriented and continuous zinc plating, a uniform and dense (101)-textured Zn layer is achieved even at a high plating capacity owing to the

rapid growth of zinc atoms along the (101) plane. As a result, the repeated zinc plating/stripping in symmetrical cells delivers a cumulative capacity of over 3000 mAh cm^{-2} with a large areal capacity of 10 mAh cm^{-2} at a current density of 10 mA cm^{-2}. Besides, the zinc plating/stripping of the Cu@PCN-coated Zn anode shows a stabilized CE of above 99.6% for 1200 cycles at 5 mA cm^{-2}, in sharp contrast to the cell with bare Zn possesses a life of merely 63 cycles and a poor CE of 97.3%. When assembled with MnO_2 cathode material to form Cu@PCN-Zn//MnO_2 full cell, it still possesses excellent capacity retention after 1200 cycles at 1 A g^{-1}. This study provides insights into the reasonable design of multifunctional interface regulation layers through coordination engineering for high-performance AZIBs.

Acknowledgements

This work was supported by the National Natural Science Foundation of China (No. 22075227) and Shaanxi Fundamental Science Research Project for Chemistry and Biology (Grant No. 23JHQ011).

Conflict of interest

There is no conflict to declare.

References

[1] a) X. Huo, X. Gong, Y. Liu, Y. Yan, Z. Du, W. Ai, *Adv. Sci.* **2024**, 11, 2309254; b)H. Meng, Q. Ran, T.-Y. Dai, J.-H. Jia, J. Liu, H. Shi, G.-F. Han, T.-H. Wang, Z. Wen, X.-Y. Lang, Q. Jiang, *Adv. Mater.* **2024**, n/a, 2403803; c)N. Yang, Y. Gao, F. Bu, Q. Cao, J. Yang, J. Cui, Y. Wang, J. Chen, X. Liu, C. Guan, *Adv. Mater.* **2024**, n/a, 2312934.

[2] a)Z. Zhao, R. Wang, C. Peng, W. Chen, T. Wu, B. Hu, W. Weng, Y. Yao, J. Zeng, Z. Chen, P. Liu, Y. Liu, G. Li, J. Guo, H. Lu, Z. Guo, *Nat. Commun.* **2021**, 12, 6606; b)H. Yang, K. Zhu, W. Xie, L. Zhang, W. Jiang, W. Li, Z. Wang, W. Yang, *Energy Environ. Sci.* **2023**, 16, 4549.

[3] a)Y. Tian, Y. An, C. Liu, S. Xiong, J. Feng, Y. Qian, *Energy Storage Mater.* **2021**, 41, 343; b)Z. Wang, J. Wang, K. Kawashima, Z. Liu, G. Henkelman, C. B. Mullins, *Angew. Chem., Int. Ed.* **2024**, n/a, e202407881; c)L. Wang, B. Zhang, W. Zhou, Z. Zhao, X. Liu, R. Zhao, Z. Sun, H. Li, X. Wang, T. Zhang, H. Jin, W. Li, A. Elzatahry, Y. Hassan, H. J. Fan, D. Zhao, D. Chao, *J. Am. Chem. Soc.* **2024**, 146, 6199; d)H. Liu, Z. Xu, B. Cao, Z. Xin, H. Lai, S. Gao, B. Xu, J.-L. Yang, T. Xiao, B. Zhang, H. J. Fan, *Adv. Energy Mater.* **2024**, n/a, 2400318.

[4] F. Ling, L. Wang, F. Liu, M. Ma, S. Zhang, X. Rui, Y. Shao, Y. Yang, S. He, H. Pan, X. Wu, Y. Yao, Y. Yu, *Adv. Mater.* **2023**, 35, 2208764.

[5] A. Chen, C. Zhao, J. Gao, Z. Guo, X. Lu, J. Zhang, Z. Liu, M. Wang, N. Liu, L. Fan, Y. Zhang, N. Zhang, *Energy Environ. Sci.* **2023**, 16, 275.

[6] Y. Wang, Z. Deng, B. Luo, G. Duan, S. Zheng, L. Sun, Z. Ye, J. Lu, J. Huang, Y. Lu, *Adv. Funct. Mater.* **2022**, 32, 2209028.

[7] a)Y. Wang, T. Ren, Z. Wang, C. Liu, Y. Zhang, A. Xu, C. Chen, J. Bai, H. Wang, X. Liu, *Adv. Energy Mater.* **2024**, n/a, 2400613; b)Y. Zeng, P. X. Sun, Z. Pei, Q. Jin, X. Zhang, L. Yu, X. W. Lou, *Adv. Mater.* **2022**, 34, 2200342; c)Y. Li, Q. Zhu, M. Xu, B. Zang, Y. Wang, B. Xu, *Adv. Funct. Mater.* **2023**, 33, 2213416.

[8] S. Chen, J. Chen, X. Liao, Y. Li, W. Wang, R. Huang, T. Zhao, S. Yan, Z. Yan, F. Cheng, H. Wang, *ACS Energy Lett.* **2022**, 7, 4028.

[9] a)Z. Jin, P. Li, Y. Meng, Z. Fang, D. Xiao, G. Yu, *Nat. Catal.* **2021**, 4, 615; b)K. Lee, E. J. Kim, J. Kim, K. H. Kim, Y. J. Lee, M. J. Lee, K. Ryu, S. Shin, J. Choi, S. H. Kwon, H. Lee, J. K. Kim, B.-H. Kim, B. J. Kim, S. W. Lee, *Adv. Energy Mater.* **2024**, 14, 2303803.

[10] a)C. Zhang, J. Xie, C. Zhao, Y. Yang, Q. An, Z. Mei, Q. Xu, Y. Ding, G. Zhao, H. Guo, *Adv.*

Mater. **2023**, 35, 2304511; b)S. Tang, Q. Dang, T. Liu, S. Zhang, Z. Zhou, X. Li, X. Wang, E. Sharman, Y. Luo, J. Jiang, *J. Am. Chem. Soc.* **2020**, 142, 19308.

[11] W. Fan, P. Li, J. Shi, J. Chen, W. Tian, H. Wang, J. Wu, G. Yu, *Adv. Mater.* **2024**, 36, 2307219.

[12] a)Z. Miao, Q. Liu, W. Wei, X. Zhao, M. Du, H. Li, F. Zhang, M. Hao, Z. Cui, Y. Sang, X. Wang, H. Liu, S. Wang, *Nano Energy* **2022**, 97, 107145; b)X. Song, L. Bai, C. Wang, D. Wang, K. Xu, J. Dong, Y. Li, Q. Shen, J. Yang, *ACS Nano* **2023**, 17, 15113.

[13] J. Ruan, D. Ma, K. Ouyang, S. Shen, M. Yang, Y. Wang, J. Zhao, H. Mi, P. Zhang, *Nano-Micro Lett.* **2023**, 15, 37.

[14] Z. Liu, Z. Guo, L. Fan, C. Zhao, A. Chen, M. Wang, M. Li, X. Lu, J. Zhang, Y. Zhang, N. Zhang, *Adv. Mater.* **2024**, 36, 2305988.

[15] Y. Su, L. Xu, Y. Sun, W. Guo, X. Yang, Y. Zou, M. Ding, Q. Zhang, C. Qiao, S. Dou, T. Cheng, J. Sun, *Small* **2024**, 20, 2308209.

[16] Z. Cheng, K. Wang, J. Fu, F. Mo, P. Lu, J. Gao, D. Ho, B. Li, H. Hu, *Adv. Energy Mater.* **2024**, 14, 2304003.

[17] J. Shen, C. Luo, S. Qiao, Y. Chen, Y. Tang, J. Xu, K. Fu, D. Yuan, H. Tang, H. Zhang, C. Liu, *ACS Catal.* **2023**, 13, 6280.

[18] a)Y. Wang, X. Jiang, G. Fu, Y. Li, Y. Tang, J.-M. Lee, Y. Tang, *ACS Appl. Mater.* **2019**, 11, 34869; b)B. Qiao, J. Zhu, Y. Liu, Y. Chen, G. Fu, P. Chen, *CrystEngComm* **2019**, 21, 3654.

[19] L. Luo, X. Xiao, Q. Li, S. Wang, Y. Li, J. Hou, B. Jiang, *ACS Appl. Mater.* **2021**, 13, 58596.

[20] W. Zhang, Q. Yao, C. Wang, R. Feng, N. Chen, J. Zhu, Z. Li, *Adv. Funct. Mater.* **2024**, 34, 2303590.

[21] Y. Zeng, Z. Pei, D. Luan, X. W. D. Lou, *J. Am. Chem. Soc.* **2023**, 145, 12333.

[22] W. Zhang, M. Dong, K. Jiang, D. Yang, X. Tan, S. Zhai, R. Feng, N. Chen, G. King, H. Zhang, H. Zeng, H. Li, M. Antonietti, Z. Li, *Nat. Commun.* **2022**, 13, 5348.

[23] J. H. Park, C. Choi, J. B. Park, S. Yu, D.-W. Kim, *Adv. Energy Mater.* **2024**, 14, 2302493.

[24] K. Guan, L. Tao, R. Yang, H. Zhang, N. Wang, H. Wan, J. Cui, J. Zhang, H. Wang, H. Wang, *Adv. Energy Mater.* **2022**, 12, 2103557.

[25] H. Liu, Z. Xin, B. Cao, Z. Xu, B. Xu, Q. Zhu, J.-L. Yang, B. Zhang, H. J. Fan, *Adv. Funct. Mater.* **2024**, 34, 2309840.

[26] H. Li, Y. Ren, Y. Zhu, J. Tian, X. Sun, C. Sheng, P. He, S. Guo, H. Zhou, *Angew. Chem., Int.*

Ed. **2023**, 62, e202310143.

[27] H. Zhang, Y. Zhong, J. Li, Y. Liao, J. Zeng, Y. Shen, L. Yuan, Z. Li, Y. Huang, *Adv. Energy Mater.* **2023**, 13, 2203254.

[28] J. Yu, C. Chen, F. Shi, R. Li, F. Chen, J. Tang, K. C. Chan, Z.-L. Xu, *Energy Storage Mater.* **2023**, 63, 102966.

[29] T. Wang, P. Wang, L. Pan, Z. He, L. Dai, L. Wang, S. Liu, S. C. Jun, B. Lu, S. Liang, J. Zhou, *Adv. Energy Mater.* **2023**, 13, 2203523.

[30] a)H. Li, Z. Wang, L. Dang, K. Yu, R. Yang, A. Fu, X. Liu, Y.-G. Guo, H. Li, X. S. Zhao, *Energy Storage Mater.* **2024**, 103547; b)H. Li, Z. Wang, L. Dang, K. Yu, R. Yang, A. Fu, X. Liu, Y.-G. Guo, H. Li, *Small* **2024**, 20, 2307722.

[31] X. Zhu, X. Li, M. L. K. Essandoh, J. Tan, Z. Cao, X. Zhang, P. Dong, P. M. Ajayan, M. Ye, J. Shen, *Energy Storage Mater.* **2022**, 50, 243.

[32] J. B. Park, C. Choi, S. W. Jung, B. C. Min, J. H. Park, D.-W. Kim, *Adv. Mater.* **2024**, 36, 2308684.